Korean J. Chem. Eng., 37(8), 1295-1305 (2020)
DOI: 10.1007/s11814-020-0569-3

pISSN: 0256-1115
eISSN: 1975-7220

INVITED REVIEW PAPER

Computational approaches to the exsolution phenomenon in perovskite oxides with a view to design highly durable and active anodes for solid oxide fuel cells

Kyeounghak Kim‡, Chaesung Lim‡, and Jeong Woo Han†

Department of Chemical Engineering, Pohang University of Science and Technology (POSTECH), Pohang, Gyeongbuk 37673, Korea

(*Received 4 April 2020 • Revised 29 April 2020 • Accepted 5 May 2020*)

Abstract−Computational approaches have been used effectively in material design for solid oxide fuel cells (SOFCs). As a way to improve the performance and stability of anode materials in SOFCs, the exsolution phenomenon has been extensively taken advantage of. In the exsolution process, highly active and stable nanoparticles (NPs) are formed uniformly over the surface of the host oxide due to the anchoring effects of exsolved NPs in the host's structure. In this review, we particularly focus on how computational approaches such as density functional theory calculation, phase field modeling, and analytic methods can be used to understand the exsolution phenomenon; this knowledge can then be exploited to design enhanced anode materials for SOFCs. We first review the nature of exsolution and then look into catalytic applications of exsolved NPs. From this point, we investigate how to engineer exsolved nanoparticles to maximize their catalytic activity with a view that any enhanced performance will aid future applications.

Keywords: Exsolution, Solid Oxide Fuel Cells (SOFCs), Perovskite Oxides, Computational Modeling, Density Functional Theory (DFT)

INTRODUCTION

Solid oxide fuel cells (SOFC) are energy converters that produce electricity from chemical energy sources. Due to the wide variety of fuels available to SOFCs, such as H_2, fossil fuel, biomass [1-3], as well as their high energy conversion efficiency (~60%) [4], SOFC is expected to be a technology used in a wide range of next generation applications from the power generator for hydrogen vehicles to an alternative for thermal power plants [5,6]. In addition, an SOFC can be a solid oxide electrolyzer cell (SOEC) that is operated in reverse; that is, acting as an SOFC the system uses fuel to produce electricity, while acting as an SOEC the system uses energy to produce fuel. This reversible, flexible nature is essential in a renewable energy system, and it complements the temporal and spatial imbalance between supply and demand of renewable energies [7].

Conventional SOFCs consist of anode, cathode, and electrolyte. The anode and cathode are in contact with the fuel and air, respectively. Oxygen ions created by an oxygen reduction reaction (ORR) at the cathode are transported to the anode where a fuel oxidation reaction through the electrolyte layer between the two electrodes occurs. As a result, electrons move from the anode to the cathode and through an external circuit, creating a current travelling in the opposite direction to the oxygen ions.

The performance of any SOFC is mainly determined by the materials used in each component. Among these, electrodes are important active layers where electrochemical reactions occur. The level of electric and ionic conductivity as well as catalytic activity are factors that determine the performance, in terms of measures such as energy conversion efficiency and power density, of the SOFC [1]. Besides these considerations, due to the high operation temperature of SOFCs, the thermal expansion coefficient as well as the chemical compatibility of the electrolyte and both electrodes are also important factors in the long term stability and durability [8,9].

For the cathode, perovskite-type materials satisfy the necessary conditions mentioned above. Co-based perovskites ($La_{1-x}Sr_xCoO_3$, $La_{1-x}Sr_xCo_{1-y}Fe_yO_3$, $Pr_{1-x}Sr_xCo_{1-y}Fe_yO_3$, and $Sm_{0.5}Sr_{0.5}CoO_3$) have higher oxygen reduction activity and electric/ionic conductivity than Co-free perovskites [10-13]. However, due to the high Co cost and the higher thermal expansion coefficient of Co-based perovskites compared to other components of SOFCs, Co-free perovskites have also been investigated for use in SOFCs [14]. Among the Co-free perovskites, Sr-doped perovskites ($Pr_{0.8}Sr_{0.2}FeO_3$, $La_{0.8}Sr_{0.2}FeO_{3-\delta}$, and $La_{0.6}Sr_{0.4}Fe_{0.9}Nb_{0.1}O_{3-\delta}$) are known to have high electric conductivity over 100 $S \cdot cm^{-1}$ at high temperature; however, the rapid decrease of their electric conductivity at intermediate temperatures remains a challenge [15-17]. In addition to the intrinsic material property such as electric conductivity, suppressing Sr segregation in Sr-based cathodes is also an important challenge to improve the cathode stability because the segregation may change structure and composition of the perovskite surfaces [18].

On the other hand, for the anode, Ni-YSZ is the material generally used because its low cost and high catalytic activity make it excellent for fuel oxidation. However, owing to its direct contact with various fuels, Ni-YSZ has various stability issues, including sulfur poisoning, carbon deposition (coking), and Ni coarsening (Fig. 1) [19]. Therefore, there have been many attempts to find an alternative anode material. Despite the development of nickel-free

†To whom correspondence should be addressed.
E-mail: jwhan@postech.ac.kr
‡K. Kim and C. Lim contributed equally to this work.

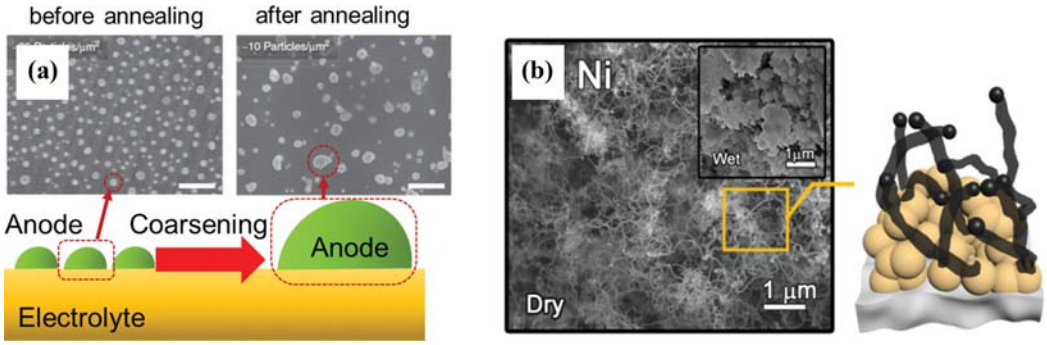

Fig. 1. (a) Scanning electron microscope (SEM) image of vapor-deposited nickel nanoparticles on $La_{0.4}Sr_{0.4}TiO_3$ before and after annealing (650 °C 24 h, and 800 °C 6 h). Scale bar is 500 nm. (reproduced from Ref. [25] with permission). (b) SEM image of carbon coking on infiltrated nickel nanoparticles. Schematic illustrations show (a) nickel coarsening and (b) carbon coking processes, respectively (reproduced from Ref. [26] with permission).

anodes including perovskite-type materials ($La_{0.8}Sr_{0.2}Cr_{0.98}Ru_{0.02}O_3$, $Sr_2FeNb_{0.2}Mo_{0.8}O_{6-\delta}$, $LaCo_{0.3}Fe_{0.67}Pd_{0.03}O_{3-\delta}$) [20-22], and fluorite-type materials ($Sc_{0.1}Y_{0.1}Zr_{0.6}Ti_{0.2}O_{1.9}$, $Ti_{0.34}Nb_{0.66}O_2$) [23,24], nickel is still fundamental for the development of the current generation of low cost and high performance SOFCs.

In this situation, the computational approach is essential for the rational design of SOFC materials. Generally, it takes about 40 hours to fabricate one SOFC test sample [27]. Performance tests, such as for long-term stability, can take up to several days. Therefore, it is not possible to test all of the candidate materials experimentally. As first-principles calculations, density functional theory (DFT) has been widely used in material design to model catalytic reactions. It can be used to find new catalytic materials through testing an enormous number of material combinations (screening) or for analyzing material properties down to the electronic structure level.

Jacobs et al. used this method to explore the best materials for use as an SOFC cathode. Using DFT calculations, they examined 2145 distinct perovskite materials using three criteria: oxygen *p*-band center (for ORR activity), formation energy per atom in ORR (for stability), and band gap (for eliminating insulator). Finally, they suggested the three best materials to be tested in experiments [28]. The screening method has also been used to design anode materials. Hwang et al. suggested that a Ni-Au alloy can be a promising catalyst as the sulfur-tolerant SOFC anode. They selected six dopant candidates (Cu, Rh, Pd, Ag, Pt, and Au) for Ni surface which have favorable surface segregation among 14 transition metals and then calculated the adsorption and dissociation energies of H_2S and the intermediates on those Ni-based alloy surfaces [29]. The effectiveness of this screening method in finding a desired material was verified by Vernoux et al's following experimental results which demonstrated high sulfur tolerance of the Ni-Au alloy [30]. In addition, Cho et al. conducted DFT-based microkinetic analysis on the H_2O/CO_2 co-electrolysis reaction on transition metal surfaces and proposed catalytically active metal alloys (Ni_3Ru, Ni_3Fe, and Ni_3Co) for use as the fuel electrode in solid oxide electrolyzer cells [31].

In addition, the computational approach can provide insight for the material design strategy in SOFCs. To overcome the stability problem caused by A-site cation segregation at SOFC cathodes, Kwon et al. reported on the relation between cation segregation and elastic energy in La-based perovskite. Using DFT calculations, they controlled the elastic energy with different sizes of B-site cation to show that A-site cation segregation can be reduced through the minimization of elastic energy [32]. In further work, they verified the strain effect through investigating experimentally strain-controlled $SrTi_{0.5}Fe_{0.5}O_{3-\delta}$ films [33].

The combination of highly active metal nanoparticles (NPs) and stable oxide support can have a synergetic effect to help fabricate better SOFC anodes that have high catalytic activity and good stability. Exsolution is a prospective method to produce stable, well dispersed metal NPs on perovskite surface. In this method, the metal NPs come from the inside of the perovskite support to its surface. This unique fabrication method produces exsolved NPs that are more stable than the NPs fabricated by conventional methods such as deposition and infiltration. Similar to how infiltration has been considered for SOFC applications, exsolution has been studied for its optimization and application to SOFC. However, compared to the many review papers that specialize in infiltration, exsolution has often been treated cursorily in review papers dealing with SOFC nanotechnology or SOFC anodes [34-36]. Especially, there is no review paper that gives an overview or summarizes the theoretical and computational approaches to the exsolution phenomena.

In this paper, we specifically focus on reviewing the computational aspects of exsolution research. In the next section, we will introduce the exsolution phenomenon and explain its application to SOFC. In section 3, the key conditions for exsolution that have been studied both experimentally and theoretically will be discussed. In section 4, computational approaches to analyze exsolution will be given an overview. Then, examples of engineered exsolution inspired by computational methods will be introduced. Finally, we discuss how to model an exsolved metal NP and simulate its growth using computational and analytical methods.

EXSOLUTION AND ITS APPLICATION TO SOFC

Exsolution is an attractive technology as it produces stable and well-dispersed metal NPs, which can be used as a catalytic active site in various chemical applications, such as chemical sensors, CO oxidation, SOFC, and so on. In the exsolution process that is mainly applied to perovskite support, metal NPs (B-site metal) are moved

from the inside of the support to its surface in the reducing condition (Fig. 2(a)). The simple fabrication process and material flexibility to the other metal oxides are the additional advantages of exsolution for its application in electrochemical devices [37]. With the recent interest in exsolution being used in these various applications, the number of papers and citations related to "exsolution" have increased

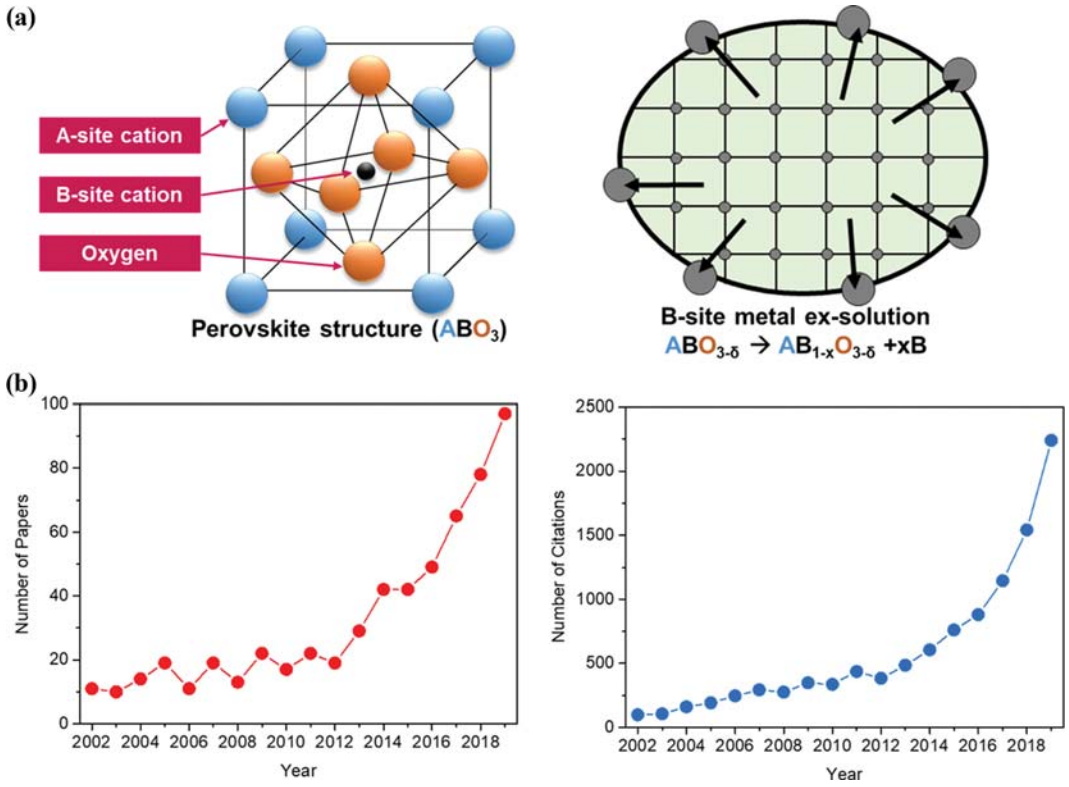

Fig. 2. (a) Schematic illustrations of perovskite structure and B-site metal exsolution in the structure, respectively. (b) Growing number of papers and citations that were searched in web of science with exsolution-related keywords.

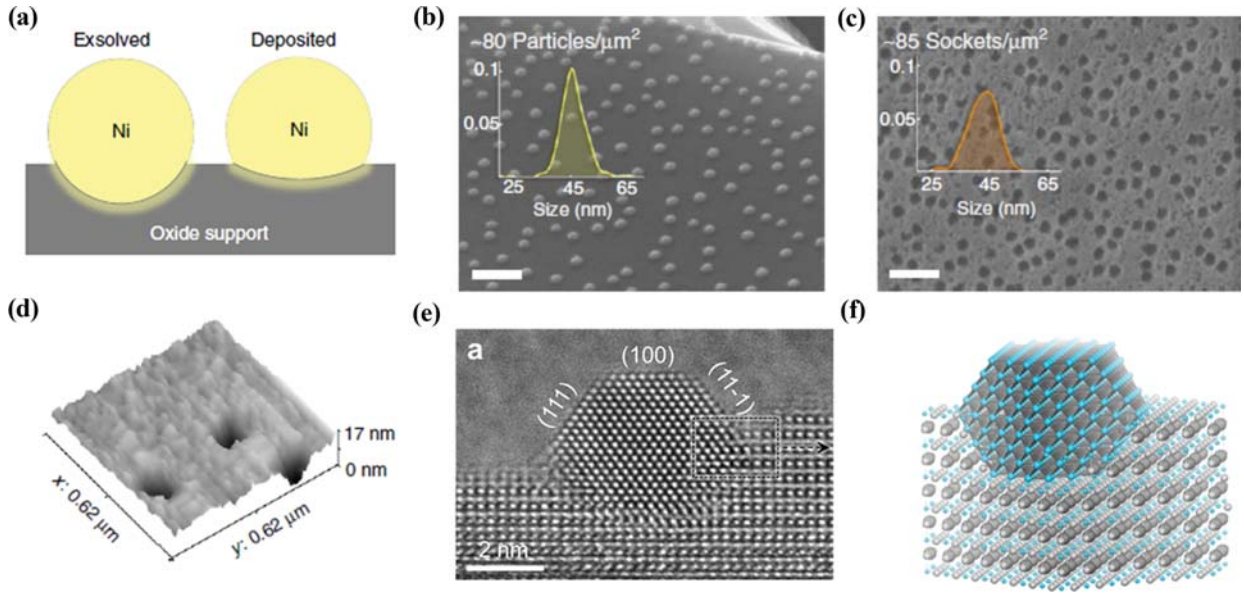

Fig. 3. (a) Schematic illustration of exsolved and deposited nanoparticles. (b), (c) SEM images of exsolved nickel nanoparticles and nano-sockets after all the nickel nanoparticles were removed by etching with HNO_3, respectively. (d) 3D AFM image of the nano-sockets in (c). (reproduced from Ref. [25] with permission). (e) Environmental transmission electron microscope (ETEM) image of a Ni nanoparticle grown from $La_{0.43}Ca_{0.37}Ti_{0.94}Ni_{0.06}O_3$ (LCTN) under vacuum at 900 °C. (f) 3D model constructed based on the crystallographic relationships highlighted in (e) (reproduced from Ref. [39] with permission).

exponentially (Fig. 2(b)).

In 2007, Madsen et al. reported on improved stability of SOFCs coming from the application of exsolved NPs to the anode [38]. The application of the exsolved Ru and Ni NPs to the $La_{0.8}Sr_{0.2}CrO_3$ anode not only increased the maximum power density compared to the SOFC with a bare $La_{0.8}Sr_{0.2}CrO_3$ anode, but also improved its long term stability. The cell was able to maintain its voltage for nearly 50 hours at intermediate temperatures of 700-800 °C in contrast to the initial or gradual cell voltage decreases experienced by a recently developed Ni-based anode under the same conditions. This result was a big surprise in the field of SOFCs.

The stability of exsolved NPs comes from their specific anchored structure. Exsolved NPs, produced by B-site metal moving from bulk to surface, are embedded in the perovskite surface (Fig. 3(a)). Dragos et al. showed the anchored structure of the exsolved NPs with an AFM image with socket-like holes on the perovskite surface after etching the exsolved Ni NPs (Fig. 3(b)-(c)) [25]. They showed an even clearer image of the embedded exsolved NPs in their other paper [39]. Their atomic resolution TEM image showed that about half of the Ni NPs are located below the perovskite surface (Fig. 3(d)-(f)). They also performed carbon coking and thermal stability tests to show the stability of the exsolved Ni NPs and compared the results to those from deposited NPs on the same perovskite surface ($La_xSr_{1-3x/2}TiO_3$). In the coking test with a CH_4/H_2 environment, the two samples showed different carbon growth mechanisms (Fig. 4). The deposited NPs were accompanied by long carbon fiber, whereas the exsolved NPs had negligible length of associated fiber (Fig. 4(b)-(d)). In addition, the growth direction of the carbon fiber in the two samples was obviously different (base growth vs. tip growth, Fig. 4(a)).

Previously, Gohier et al. reported that the carbon growth direction on NP metal catalysts was controlled by the interaction between the NPs and the support [40]. Thus, a strong interaction between the exsolved NPs and perovskite surface was considered to be the reason for high coking resistance. In the thermal stability test, the exsolved Ni NPs also showed high thermal stability (similar particle size and distribution were maintained for 90 hours at 900 °C) compared with the coalescing of the deposited Ni NPs after 6 hours at 800 °C.

Regeneration is another important characteristic of exsolved NPs. The exsolved NPs fabricated by a reducing process can resolve back into perovskite bulk in oxidation condition. This redox process can be repeated continuously (Fig. 5), which improves the redox stability of SOFCs. Kim et al. recently reported on the high redox stability of SOFC anodes made with exsolved Ni NPs [27]. In a ten redox cycle test at 750 °C, the specific resistance of the anode only increased 0.027 Ω·cm^2 (1.79 Ω·cm^2 increase was seen without exsolved NPs).

After the work of Madsen et al., other catalytically active metal NPs (Fe, Ni-Fe alloy, Co, Ni-Co alloy, Cu, Ni-Cu alloy, Ag, Pd, and so on) have been investigated to see if it is possible to apply the exsolution method [41-48]. Although it is simple to fabricate well-dispersed metal NPs on oxide support, some metals such as Fe require a particular support oxide and difficult reducing condition to be easily exsolved. In a similar way to the material design for SOFCs, it is impossible to perform optimization and device testing on all possible exsolved NP candidates experimentally. Therefore, the com-

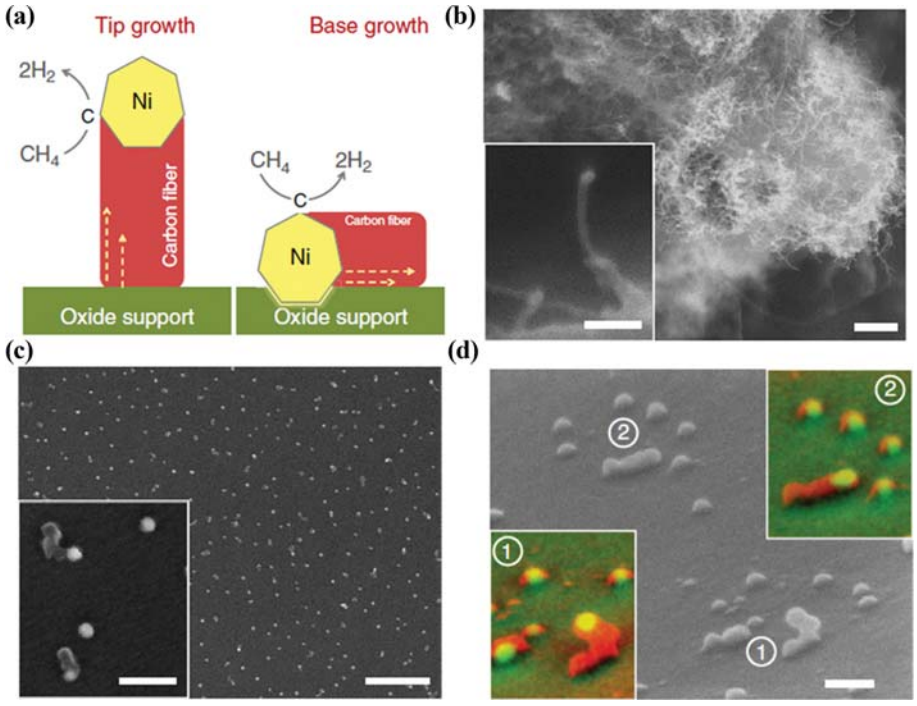

Fig. 4. (a) Schematic illustration of carbon fiber growths depending on the conditions of nickel nanoparticles. (b) SEM image of carbon coking on infiltrated nickel nanoparticles. Scale bars are 1 μm in overview and 100 nm in inset figures. (c) SEM image of carbon coking on exsolved nickel nanoparticles. Scale bars are 500 nm in overview and 100 nm in inset figures. (d) Side view image of SEM image in (c). Scale bar is 100 nm (reproduced from Ref. [25] with permission).

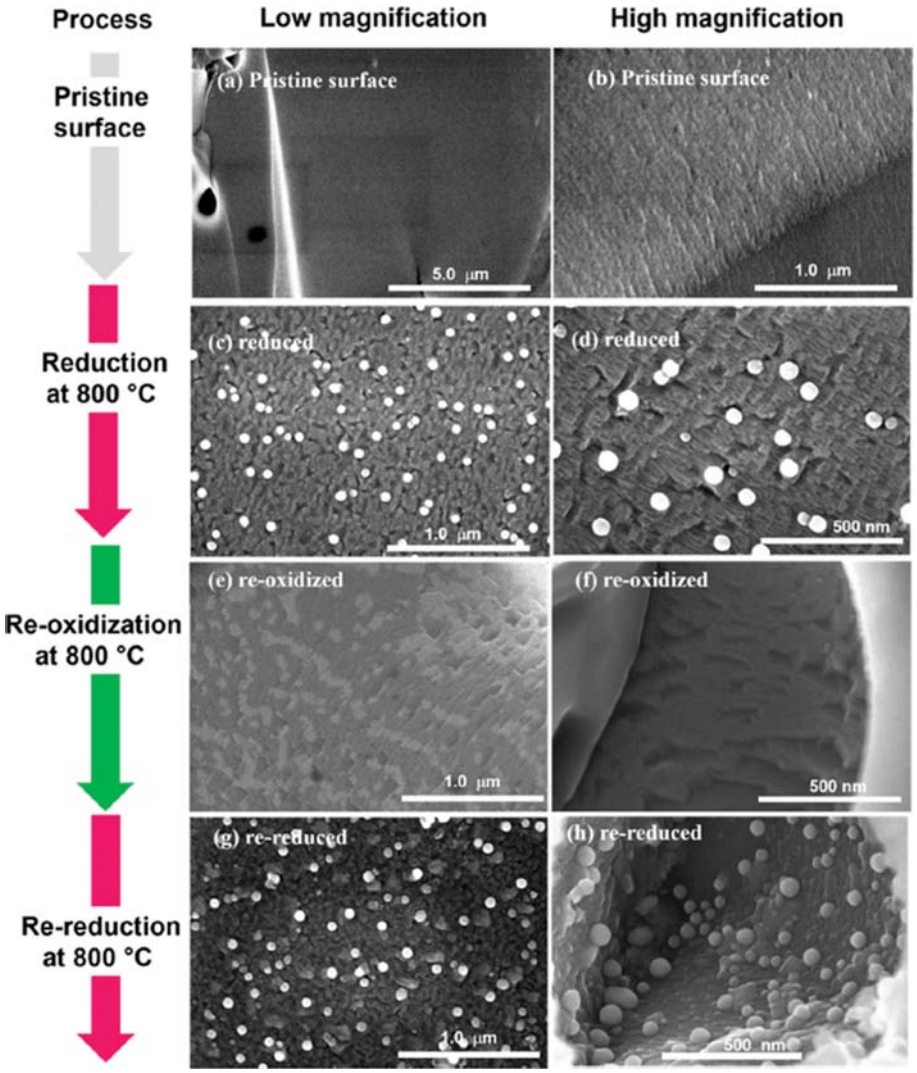

Fig. 5. SEM images of $La_{0.3}Sr_{0.7}Cr_{0.3}Fe_{0.6}Co_{0.1}O_{3-\delta}$ perovskite during redox processes at 800 °C. The sphere nanoparticles at each reduction condition are the exsolved cobalt nanoparticles (reproduced from Ref. [49] with permission).

putational approach is required to quickly predict which combination of metal and support will lead to the facile exsolution of metal NPs. In addition, it has also been widely used for mechanistic study of the exsolution process. In the following section, we will review the computational approaches used to investigate exsolution.

MECHANISTIC ANALYSIS OF EXSOLUTION

Although the underlying mechanism of exsolution is still not clear, several possible elementary steps in the exsolution process have been proposed through previous experiments and theoretical analyses. One proposed mechanism is the defect-mediated exsolution suggested by Dragos et al. (five point-defect reactions, Fig. 6(a)). They demonstrated that the amount of exsolved NPs on $La_{0.4}Sr_{0.4}Ni_xTi_{1-x}O_{3-\delta}$ surface increased with A-site defect concentration [50,51]. The main reasons for this boosted Ni exsolution have been suggested to be (1) the formation of A-site defects changes the number of oxygen vacancies to maintain the stoichiometry of ABO_3 perovskite (Eq. (1)), (2) the reducing environment then increases the number of oxygen vacancies (Eq. (2)), and thus (3) metal atoms are reduced from oxide phase to the metallic phase through B-metal exsolution (Eq. (3)) or reduction of MO (Eq. (5)) followed by the exsolution of Schottky defects (Eq. (4)) (Fig. 6(a)). In this mechanism, the degree of exsolution is limited under a certain threshold of oxygen vacancies (δ_{lim}), which is required at least to maintain the perovskite structure (Fig. 6(b)) [51]. Sun et al. also proposed two exsolution mechanisms (Fig. 6(c)): the formation of oxygen vacancies under reducing environments destabilizes the lattice structure, which induces the exsolution of B-site cations (Way 1), and both oxygen vacancies and B-cation complex defects such as Schottky defects result in B-cation exsolution (Way 2) [52]. Jiang et al. used phase field modeling to kinetically analyze the exsolution phenomenon on a perovskite surface (non-equilibrium thermodynamics) [53]. Their simulation suggested that spinodal decompositions depending on the reducing condition, A-site deficiency, and segregation energy trigger exsolution.

Combining the above results, the dopant segregation towards the surface (B-metal segregation) and reduction of the segregated

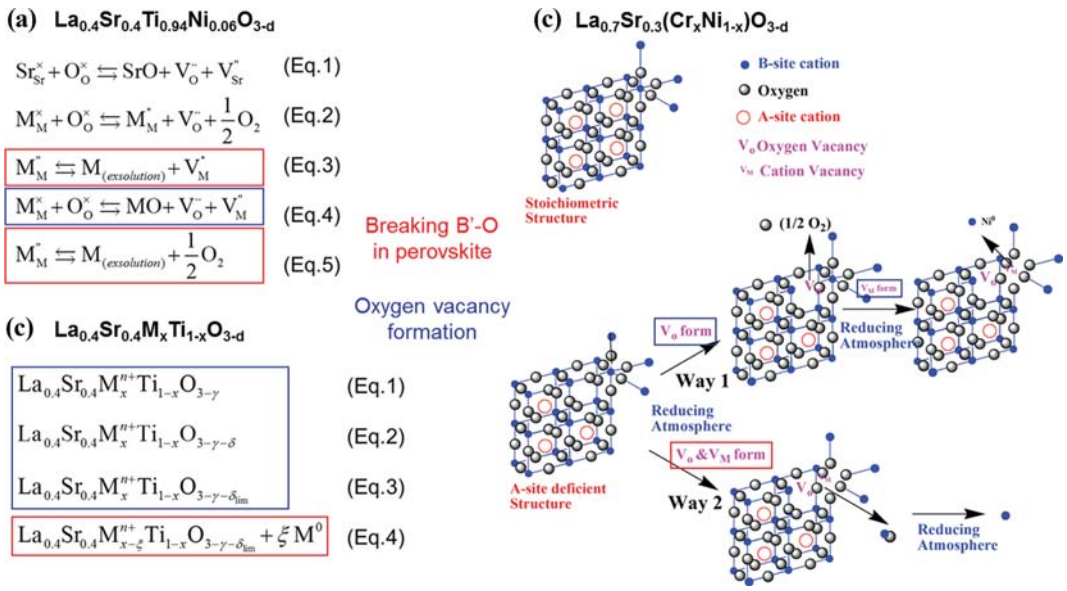

Fig. 6. Experimentally suggested key elementary steps for B-metal exsolution (reproduced from Ref. [52] with permission).

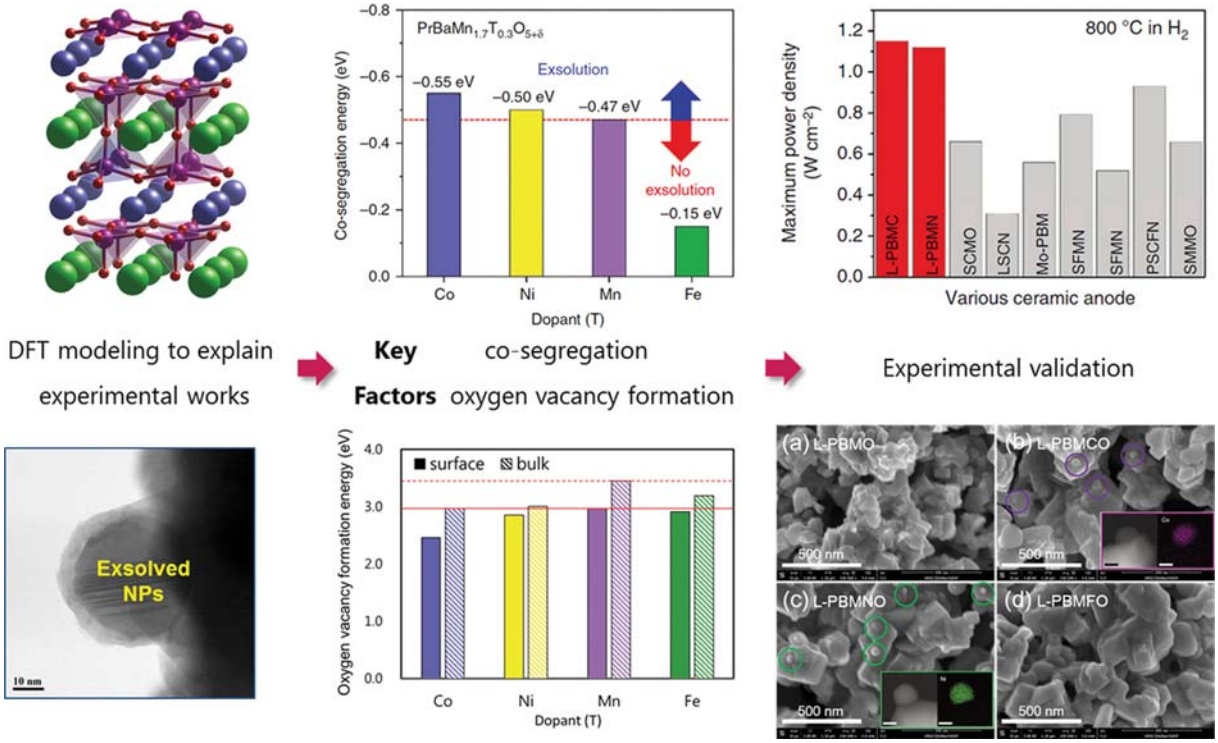

Fig. 7. Research scheme for the simulation driven material design of exsolved NPs (reproduced from Ref. [54] with permission).

dopant (breaking the bond between the oxygen and B-metal) can be seen as the key factors for exsolution. Kwon et al. confirmed the validity of these key factors by predicting exsolution tendencies [54]. Using the DFT method, co-segregation energies were calculated for the layered perovskite structure of $PrBaMn_{1-x}T_xO_{5-\delta}$ (T=Mn, Co, Ni, and Fe) (L-PBTMO) (Fig. 7). The segregation of a dopant atom (T) with an oxygen vacancy, which is defined as co-segregation energy, was used to describe dopant segregation under a reducing environment, in which oxygen vacancies are easily formed. Co and Ni showed higher co-segregation energies than the host Mn, whereas Fe showed lower co-segregation energy; this implies that Co and Ni exsolutions from the host perovskite of L-PBTMO are more favorable than from the host Mn while Fe is less favorable. The experimental results also confirmed that after reduction treatments, the exsolved Co and Ni NPs were observed at the Co and Ni doped L-PBMO (L-PBMCO and L-PBMNO), respectively. No

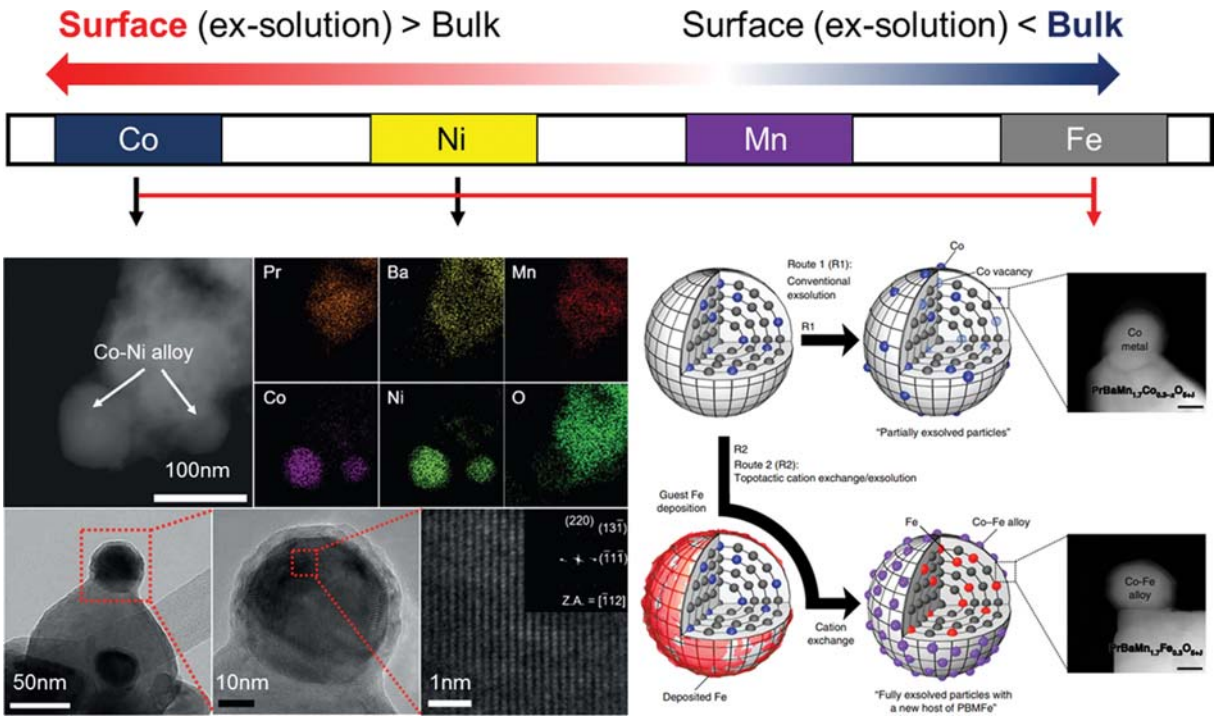

Fig. 8. Engineering of B-metal exsolution. The left inset figures are TEM and EDS map of the exsolved Co-Ni alloy NPs on $PrBaMn_{1.7}Co_{0.1}Ni_{0.2}O_{5+\delta}$. The right inset figure is a schematic illustration of topotatic exchange-driven boost for Co exsolution (reproduced from Ref. [60] with permission).

exsolved NPs were observed at the pure (L-PBMO) and Fe doped L-PBMO (L-PBMFO). The segregation energies also explained the tendency of Ni exsolution on different $(La_{0.5}Sr_{0.5})(Sc_{1-x}Ni_x)O_3$ surfaces of (100), (010), (001), and (121). The most preferential exsolution of Ni NPs was observed on the (010) surface, which can be explained by its higher segregation energy than any other surfaces [55].

Once segregation occurs, the segregated metals should decompose (be reduced) from oxide phase to metallic phase. This can be proceeded by the formation of oxygen vacancies near the segregated metals, which can be measured by surface oxygen vacancy formation energy obtained from the DFT calculations. The oxygen vacancy formation energy also shows that Co and Ni form oxygen vacancies more easily than the host Mn or Fe dopant [54]. Consequently, the synthesized electrode materials of L-PBMCO and L-PBMNO with the exsolved NPs showed the higher power density that came with long term stability than any other promising ceramic electrode materials up to 2017. These results demonstrate that computational approaches are able to capture the main characteristics of B-metal exsolution, thereby playing an important role in designing exsolution materials as well as elucidating the mechanism at the atomic scale (Fig. 7).

ENGINEERING OF EXSOLUTION TENDENCY

From the above results, we learned two main things about the exsolution phenomenon: (1) Exsolution requires a large enough driving force for the target element to be exsolved from the host structure. (2) However, each dopant element has a thermodynamically different degree of driving force (e.g., different dopant-oxygen vacancies, co-segregation energy, and so on) (Fig. 7). By considering these two characteristics, exsolution can be effectively engineered for various purposes. In practical applications, theory-guided experimental results have demonstrated the alloy exsolution of Co-Ni bimetallic NPs (Fig. 8). To elucidate the mechanism of alloy exsolution, the energy requirements for two possible paths (surface alloy formation and bulk alloy formation) were calculated. The surface alloy formation path starts with the individual segregation of Co-O_v and Ni-O_v toward the surface (ΔG=−0.46 eV). Then, they form the nearest neighbored Co-O_v-Ni complex at the surface (ΔG=−0.01 eV). On the other hand, the bulk alloy formation path starts with the formation of the nearest neighbored Co-O_v-Ni complex in bulk (ΔG=+0.02 eV), and then it segregates together toward the surface (ΔG=−0.48 eV). In both paths, the alloy formation requires thermodynamically higher energies than segregation. In particular, a surface alloy formation path was revealed to be a thermodynamically more favorable process than the bulk alloy formation path because it has no apparent thermodynamic energy requirements. A similar approach was used to explain the exsolution of Co-Fe alloy on Co doped $Sr_2Fe_{1.5}Mo_{0.5}O_{6-\delta}$ (SFM). The introduction of Co defects created by Co exsolution with oxygen vacancies decreases the segregation energy of Fe from 0.91 eV to 0.62 eV, which facilitates Fe exsolution to form exsolved Co-Fe alloy NPs on SFM [56].

Exsolved alloy NPs showed good catalytic activity as well as long-term stability for both CO_2 electrolysis [56] and fuel oxidation in SOFC anodes [57]. Generally, alloy metal catalysts tend to have unique catalytic activity for several reasons. First, they have unique

electronic structures. For example, Ko et al. showed that surface electronic structure (*d*-band center) of binary *d*-block transition metal catalysts was tuned by the electronic structure of the constituent elements [58]. Thus, a unique electronic structure, which is not present in a monometallic catalyst, can be achieved by well-designed multi-component alloying. Second, alloys can provide various active sites for surface reactions as a bifunctional catalyst. Each element in an alloy catalyst selectively provides the active sites for different kinds of reactants [59].

Although extrinsic factors such as oxygen partial pressure and temperature can be used to increase the total amount of exsolved NPs, at some point the numbers become limited by both dopant concentration and the solubility limit to maintain the perovskite structure. To overcome this, topotatic ion exchange was suggested (Fig. 8) [60]. The main concept of topotatic ion exchange is an exchange between externally provided cations and doped cations in the bulk perovskite. For example, Co prefers to segregate toward the L-PBTMO surface, whereas Fe does not. Therefore, the cations externally provided by means of infiltration, which prefer to dissolve from surface to the bulk, fill up the B-site vacant sites created by Co exsolution, preserving the bond networks in the perovskite structure. This process may be able to maximize the amount of exsolved Co NPs. To prove this hypothesis, the energy requirements for the incorporation of Fe into perovskite surface and the exchange of incorporated Fe with bulk Co were calculated. Both incorporation and exchange are thermodynamically favorable with negative reaction energies of −0.41 eV and −0.34 eV, respectively. In addition, the Fe-Co exchange energy increases as the amount of incorporated Fe increases. These computational results are in good agreement with the experimental result that showed a large amount of exsolved NPs being obtained under Fe infiltration onto $PrBaMn_{1.7}Co_{0.3}O_{5+\delta}$. About five-times more exsolved NPs were observed at 12 wt% of Fe infiltrated PBMCO than without Fe infiltration in a given area. The maximum power density at 800 °C in H_2 achieved the best performance among the promising ceramic anode materials up to 2019. This implies that engineering of exsolution properties is a good strategy for designing high performance anode materials in SOFCs.

Lattice strain can also be applied to engineer the ideal degree of exsolution. The degree of Ni exsolution on $La_{0.2}Sr_{0.7}Ni_{0.1}Ti_{0.9}O_{3-\delta}$ (LSNT) thin films was increased when grown on $GdScO_3$ (GSO) (110), which, with a misfit strain of +1.2%, has a higher lattice parameter than LSNT. Based on analytic modeling equations, it was reported that induced misfit-strain energy not only reduces the nucleation barrier but also increases the nucleation rate [61]. A similar concept was also applied to suppress A-site cation segregation [33]. DFT results demonstrate that each constituent in the perovskite structure has its own optimal strain state. For example, tensile strain stabilizes Sr atoms in $Sr(Ti,Fe)O_3$ because the Sr atoms are intrinsically in a compressive state at the strain-free equilibrium state of

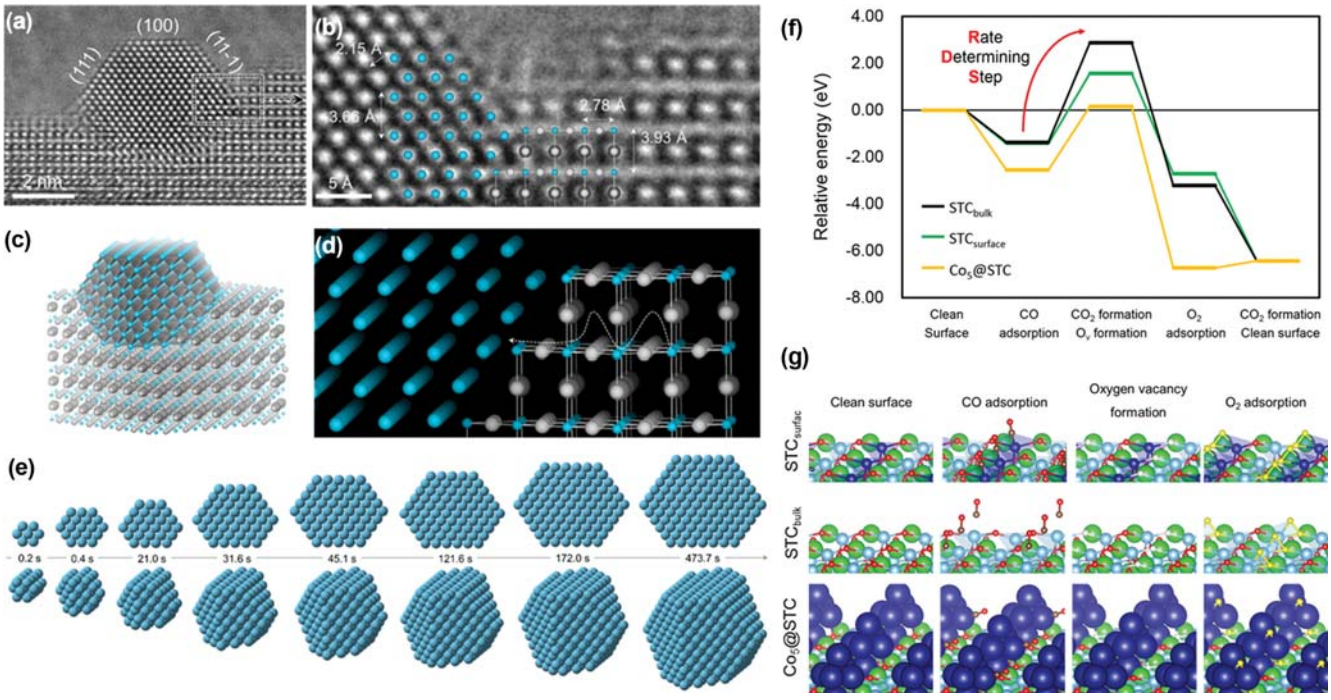

Fig. 9. (a) Environmental transmission electron microscope (ETEM) image of a Ni nanoparticle grown from $La_{0.43}Ca_{0.37}Ti_{0.94}Ni_{0.06}O_3$ (LCTN) under a vacuum at 900 °C. (b) Enlarged image of a part marked with a black rectangle in (a) that shows the particle-perovskite interface with an overlay of Ni metal and perovskite lattices in their respective orientations. This image reveals epitaxial growth. (c) 3D model constructed based on the crystallographic relationships highlighted in ((a), (b)). (d) Details of the 3D model in (c), which highlights the diffusion pathway of Ni^{2+} ions through the LCTN perovskite lattice. (e) 2D and 3D models of the time evolution of a Ni particle on LSTN during the exsolution process. (f) Relative energy diagram for the CO oxidation reaction and (g) optimized structures of the reaction intermediates at each elementary step on the Co segregated STC surface ($STC_{surface}$), the surface with Co located in bulk (STC_{bulk}) and with exsolved Co NP (Co_5@STC) (reproduced from Ref. [39] and [63] with permission).

perovskite oxide. Contrary to A-site cations (Sr), B-site cations are intrinsically in a tensile state. Therefore, it has been suggested that the tensile strain may facilitate the segregation of B-site cations by destabilizing them. This stability tuning might be a key reason for enhanced exsolution under a tensile strain state of LSNT [61].

ATOMISTIC MODELING AND CATALYTIC ACTIVITY OF EXSOLVED NANOPARTICLES

The key characteristic that is different between NPs synthesized by conventional deposition methods and exsolved NPs is the partially immersed structure of NPs into the host perovskite (Fig. 9(a)-(e)) [39]. To model these NPs at an atomic scale, identifying the interface between exsolved NPs and host perovskite structure is important. Due to the lack of known atomic structure in exsolved NPs, several possible models have been used to describe the exsolved NP. These include the non-socketed NP model (deposition model), surface doping model, and the small metal cluster incorporation model [56,62,63].

Based on these models, the catalytic activity of exsolved NPs has been further investigated (Fig. 9(f)). For CO oxidation, the active site was revealed to be at the gas-NP-support triple phase boundary (TPB) on Co exsolved $Sr(Ti_{1-x}Co_x)O_3$ by both experimental and theoretical analyses (Fig. 9(g)). In particular, DFT results demonstrated that the first CO_2 formation step in the Mars-van Krevelen (MvK) mechanism is the rate-determining step (RDS) for CO oxidation. A lower reaction barrier at RDS with strong CO adsorption was calculated for Co NPs exsolved on $Sr(Ti_{1-x}Co_x)O_3$ compared to $Sr(Ti_{1-x}Co_x)O_3$ without exsolved Co NPs; these results imply that exsolution provides not only strong metal-support interaction but also catalytically active sites for CO oxidation [63].

The higher catalytic activity of exsolved Co-Fe alloy NPs on $Sr_2Fe_{1.35}Mo_{0.45}Co_{0.2}O_{6-\delta}$ (SFMC) compared to pure SFMC was also identified by a free energy diagram for CO_2 electrolysis. In this reaction, CO_2 is more easily dissociated into CO and atomic O on the exsolved NPs due to greater charge donation of Fe to the carbon atom in CO_2. This process was revealed as RDS and healed surface oxygen vacancies [56]. However, the particle size and morphology of exsolved NPs constructed in the modeling were not still sufficient to describe the anchoring, size, and interfacial effects often observed in experiments. In this regard, more realistic models should be developed for computational simulations.

ANALYTIC MODELING OF PARTICLE GROWTH

Once the dopant atoms segregate toward the surface, nucleation and growth begin near the surface. In general, the Gibbs free energy for a certain size of particle is determined by the balance between the two competitive factors of volume (bulk) free energy and interfacial (surface) free energy. In this regard, Gao et al. developed three analytical models based on a homogeneous nucleation model: (1) strain-limited exsolution, (2) reactant-limited exsolution, and (3) diffusion-limited exsolution (Fig. 10(b)). Among the three possible models, the experimentally measured sizes of Ni NPs exsolved

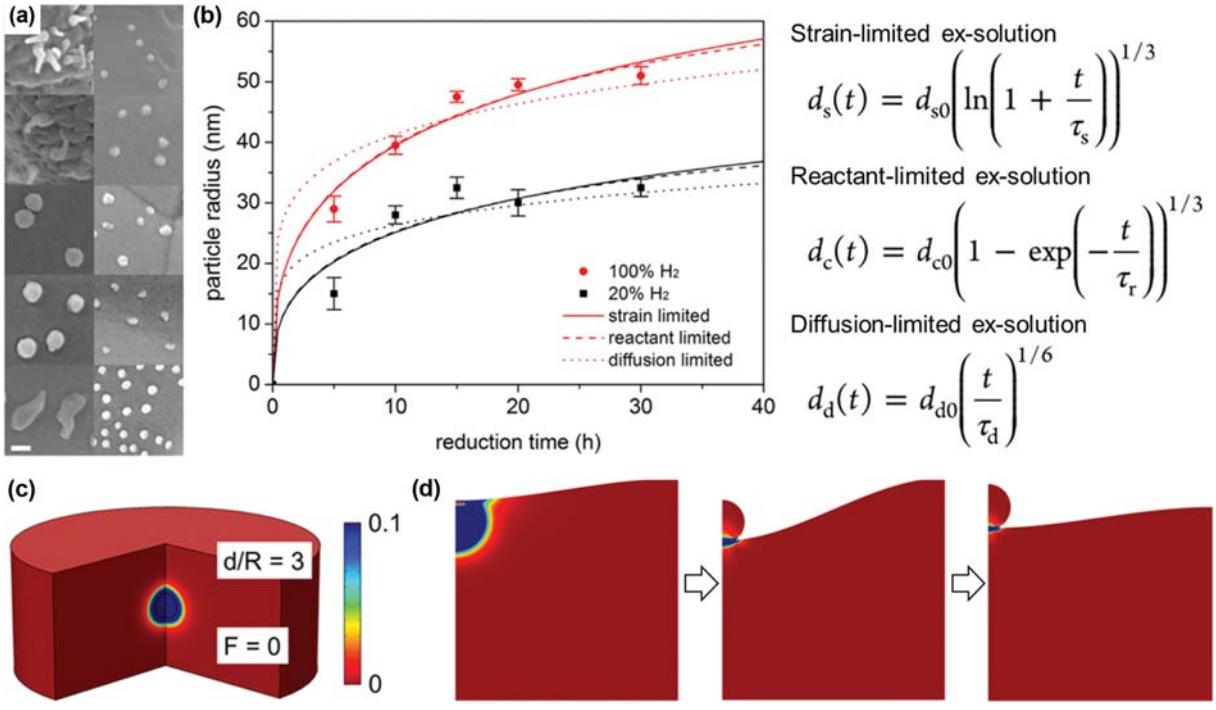

Fig. 10. (a) Particle reduction under pure (left) and 20% (right) H_2 treatment for 5, 10, 15, 20, and 30 h. (b) Average particle size and fitting curves from three prediction models as a function of reduction time. The d, t, and τ in inset equations denote particle dimension, time, and time constant, respectively. (c) The initial state of strain field simulation. Color bar denotes the distribution of volumetric free energy density. (d) Time-lapse spatial free energy density distributions as the system evolves to minimize the total free energy of the system (reproduced from Ref. [55] and [64] with permission).

on $La_{0.4}Sr_{0.4}Sc_{0.9}Ni_{0.1}O_{3-\delta}$ (LSSN) as a function of reduction time were well matched with the equation of strain- and reactant-limited models. However, several assumptions were used in their models: (1) the reaction rate is only dependent on the activation energy in strain-limited models, (2) the activation energy is fixed in reactant-limited models, and (3) the key parameters used in these models should be fitted by the experimental results [55]. Nevertheless, those models effectively described the *in-situ* growth of Co NPs on $SrTi_{0.75}Co_{0.25}O_{3-\delta}$ polycrystalline thin films [63]. To precisely predict the size, morphology, and distribution of exsolved NPs without expensive and time-consuming experiments, fundamental theory-based models that can be practically and generally applied should be further developed.

To understand the origin of the formation of socketed exsolved NPs, Oh et al. suggested an interplay between surface free energy and strain energy as the driving force for exsolution by using a macroscopic view of strain field modeling (Fig. 10(c)). As exsolution proceeds, strain energy increases (blue region) until surface deformation occurs. Then, it decreases (changes to red) at the optimal pit depth to stabilize the exsolved NP (Fig. 10(d)) [64]. In strain field modeling, however, many key factors such as surface energy of the oxide matrix and metal-oxide interface energy were simplified or taken by other similar oxide systems. Therefore, the results cannot be applied to unknown materials. In this regard, the development of a reasonable exsolution model for atomistic simulation and further research into the effect of interfacial electronic structure and of the effective strain of exsolved NPs on the catalytic activity are required.

SUMMARY AND OUTLOOK

We have introduced how to use a computational approach to design highly active and durable exsolved NPs on perovskite materials while giving several examples. As computational resources, computing speed, algorithm efficiency, and accuracy increases, the role of computational approaches becomes more important in various application fields. In particular, high throughput screening alongside elucidating reaction mechanisms at the atomic scale is established as a typical research procedure nowadays. Although the exsolution phenomenon has many advantages in the field of catalysis and electrode materials, the underlying mechanism and the origin of the high catalytic activity produced are still unclear due to the limitations of the measurable scale, complexity of reaction, and high cost in experiments. In this regard, high accuracy of computational techniques enables us to broaden our understanding of the electronic and atomic structures of the materials in detail. Although it is still not easy to cover every aspect of exsolution with only computational simulations, the effective combination of computational and experimental approaches is a useful strategy that makes up for the inherent limitations of each method through continual feedback between them [65].

ACKNOWLEDGEMENTS

The authors acknowledge the financial support from the Ministry of Trade, Industry & Energy (MOTIE) of the Republic of Korea (No. 20173020032120) and the R&D program of the Global Frontier Center for Multiscale Energy System (NRF-2014M3A6A7074784) through the National Research Foundation of Korea (NRF) funded by the Korea government (MSIT). The authors also acknowledge the supercomputing resource including technical support from Supercomputing Center/Korea Institute of Science and Technology Information (KSC-2017-C3-0028).

REFERENCES

1. J. H. Kim, Y. M. Park and H. Kim, *Korean J. Chem. Eng.*, **29**, 1541 (2012).
2. M. Liu, Y. Choi, L. Yang, K. Blinn, W. Qin, P. Liu and M. Liu, *Nano Energy*, **1**, 448 (2012).
3. D. Singh, E. Hernández-Pacheco, P. N. Hutton, N. Patel and M. D. Mann, *J. Power Sources*, **142**, 194 (2005).
4. A. M. Abdalla, S. Hossain, A. T. Azad, P. M. I. Petra, F. Begum, S. G. Eriksson and A. K. Azad, *Renew. Sust. Energy Rev.*, **82**, 353 (2018).
5. J.-Y. Lee, M. Yoo, K. Cha, T. W. Lim and T. Hur, *Int. J. Hydrogen Energy*, **34**, 4243 (2009).
6. B. Haberman, C. M. Baca and T. Ohrn, *ECS Transactions*, **35**, 451 (2011).
7. Z. Yang, J. Zhang, M. C. W. Kintner-Meyer, X. Lu, D. Choi, J. P. Lemmon and J. Liu, *Chem. Rev.*, **111**, 3577 (2011).
8. Y. Chen, W. Zhou, D. Ding, M. Liu, F. Ciucci, M. Tade and Z. Shao, *Adv. Energy Mater.*, **5**, 1500537 (2015).
9. P. I. Cowin, C. T. G. Petit, R. Lan, J. T. S. Irvine and S. Tao, *Adv. Energy Mater.*, **1**, 314 (2011).
10. F. Tietz, I. A. Raj, M. Zahid and D. Stöver, *Solid State Ionics*, **177**, 1753 (2006).
11. A. Petric, P. Huang and F. Tietz, *Solid State Ionics*, **135**, 719 (2000).
12. H. Ullmann, N. Trofimenko, F. Tietz, D. Stöver and A. Ahmad-Khanlou, *Solid State Ionics*, **138**, 79 (2000).
13. Y. M. Park and H. Kim, *Korean J. Chem. Eng.*, **30**, 2017 (2013).
14. P. Kaur and K. Singh, *Ceram. Int.*, **46**, 5521 (2020).
15. J. Piao, K. Sun, N. Zhang, X. Chen, S. Xu and D. Zhou, *J. Power Sources*, **172**, 633 (2007).
16. J. H. Kim, Y. M. Park, T. Kim and H. Kim, *Korean J. Chem. Eng.*, **29**, 349 (2012).
17. T. Yu, X. Mao and G. Ma, *J. Alloys Compd.*, **608**, 30 (2014).
18. B. Koo, K. Kim, J. K. Kim, H. Kwon, J. W. Han and W. Jung, *Joule*, **2**, 1476 (2018).
19. M. S. Khan, S.-B. Lee, R.-H. Song, J.-W. Lee, T.-H. Lim and S.-J. Park, *Ceram. Int.*, **42**, 35 (2016).
20. T. Caillot, G. Gauthier, P. Delichère, C. Cayron and F. C. S. Aires, *J. Catal.*, **290**, 158 (2012).
21. H. Ding, Z. Tao, S. Liu and Y. Yang, *J. Power Sources*, **327**, 573 (2016).
22. J. Shen, Y. Chen, G. Yang, W. Zhou, M. O. Tadé and Z. Shao, *J. Power Sources*, **306**, 92 (2016).
23. W. Liu and M. Flytzanistephanopoulos, *J. Catal.*, **153**, 304 (1995).
24. G. Pudmich, B. A. Boukamp, M. Gonzalez-Cuenca, W. Jungen, W. Zipprich and F. Tietz, *Solid State Ionics*, **135**, 433 (2000).
25. D. Neagu, T.-S. Oh, D. N. Miller, H. Ménard, S. M. Bukhari, S. R. Gamble, R. J. Gorte, J. M. Vohs and J. T. S. Irvine, *Nat. Commun.*, **6**, 8120 (2015).

26. S. Kim, C. Kim, J. H. Lee, J. Shin, T.-H. Lim and G. Kim, *Electrochim. Acta*, **225**, 399 (2017).
27. K. J. Kim, M. K. Rath, H. H. Kwak, H. J. Kim, J. W. Han, S.-T. Hong and K. T. Lee, *ACS Catal.*, **9**, 1172 (2019).
28. R. Jacobs, T. Mayeshiba, J. Booske and D. Morgan, *Adv. Energy Mater.*, **8**, 1702708 (2018).
29. B. Hwang, H. Kwon, J. Ko, B.-K. Kim and J. W. Han, *Appl. Surf. Sci.*, **429**, 87 (2018).
30. F. M. Sapountzi, C. Zhao, A. Boréave, L. Retailleau-Mevel, D. Niakolas, C. Neofytidis and P. Vernoux, *Catal. Sci. Technol.*, **8**, 1578 (2018).
31. A. Cho, J. Ko, B.-K. Kim and J. W. Han, *ACS Catal.*, **9**, 967 (2019).
32. H. Kwon, W. Lee and J. W. Han, *RSC Adv.*, **6**, 69782 (2016).
33. B. Koo, H. Kwon, Y. Kim, H. G. Seo, J. W. Han and W. Jung, *Energy Environ. Sci.*, **11**, 71 (2018).
34. J. T. S. Irvine, D. Neagu, M. C. Verbraeken, C. Chatzichristodoulou, C. Graves and M. B. Mogensen, *Nat. Energy*, **1**, 15014 (2016).
35. L. Fan, B. Zhu, P.-C. Su and C. He, *Nano Energy*, **45**, 148 (2018).
36. Y. Li, W. Zhang, Y. Zheng, J. Chen, B. Yu, Y. Chen and M. Liu, *Chem. Soc. Rev.*, **46**, 6345 (2017).
37. N. W. Kwak, S. J. Jeong, H. G. Seo, S. Lee, Y. Kim, J. K. Kim, P. Byeon, S.-Y. Chung and W. Jung, *Nat. Commun.*, **9**, 4829 (2018).
38. B. D. Madsen, W. Kobsiriphat, Y. Wang, L. D. Marks and S. Barnett, *ECS Trans.*, **35**, 1339 (2011).
39. D. Neagu, V. Kyriakou, I.-L. Roiban, M. Aouine, C. Tang, A. Caravaca, K. Kousi, I. Schreur-Piet, I. S. Metcalfe, P. Vernoux, M. C. M. Sanden and M. N. Tsampas, *ACS Nano*, **13**, 12996 (2019).
40. A. Gohier, C. P. Ewels, T. M. Minea and M. A. Djouadi, *Carbon*, **46**, 1331 (2008).
41. Y. Zhu, W. Zhou, R. Ran, Y. Chen, Z. Shao and M. Liu, *Nano Lett.*, **16**, 512 (2016).
42. Y.-F. Sun, Y.-Q. Zhang, J. Chen, J.-H. Li, Y.-T. Zhu, Y.-M. Zeng, B. S. Amirkhiz, J. Li, B. Hua and J.-L. Luo, *Nano Lett.*, **16**, 5303 (2016).
43. Y.-F. Sun, J.-H. Li, M.-N. Wang, B. Hua, J. Li and J.-L. Luo, *J. Mater. Chem. A*, **3**, 14625 (2015).
44. H. Li, G. Sun, K. Xie, W. Qi, Q. Qin, H. Wei, S. Chen, Y. Wang, Y. Zhang and Y. Wu, *Int. J. Hydrogen Energy*, **39**, 20888 (2014).
45. D. M. Bierschenk, E. Potter-Nelson, C. Hoel, Y. Liao, L. Marks, K. R. Poeppelmeier and S. A. Barnett, *J. Power Sources*, **196**, 3089 (2011).
46. H. Wei, K. Xie, J. Zhang, Y. Zhang, Y. Wang, Y. Qin, J. Cui, J. Yan and Y. Wu, *Sci. Rep.*, **4**, 5156 (2014).
47. Z. Du, H. Zhao, S. Yi, Q. Xia, Y. Gong, Y. Zhang, X. Cheng, Y. Li, L. Gu and K. Świerczek, *ACS Nano*, **10**, 8660 (2016).
48. B. Hua, N. Yan, M. Li, Y.-F. Sun, Y.-Q. Zhang, J. Li, T. Etsell, P. Sarkar and J.-L. Luo, *Adv. Mater.*, **28**, 8922 (2016).
49. K.-Y. Lai and A. Manthiram, *Chem. Mater.*, **30**, 2838 (2018).
50. D. Neagu, G. Tsekouras, D. N. Miller, H. Ménard and J. T. S. Irvine, *Nat. Chem.*, **5**, 916 (2013).
51. G. Tsekouras, D. Neagu and J. T. Irvine, *Energy Environ. Sci.*, **6**, 256 (2013).
52. Y. Sun, J. Li, Y. Zeng, B. S. Amirkhiz, M. Wang, Y. Behnamian and J. Luo, *J. Mater. Chem. A*, **3**, 11048 (2015).
53. G. Jiang, F. Yan, S. Wan, Y. Zhang and M. Yan, *Phys. Chem. Chem. Phys.*, **21**, 10902 (2019).
54. O. Kwon, S. Sengodan, K. Kim, G. Kim, H. Y. Jeong, J. Shin, Y.-W. Ju, J. W. Han and G. Kim, *Nat. Commun.*, **8**, 15967 (2017).
55. Y. Gao, D. Chen, M. Saccoccio, Z. Lu and F. Ciucci, *Nano Energy*, **27**, 499 (2016).
56. H. Lv, L. Lin, X. Zhang, Y. Song, H. Matsumoto, C. Zeng, N. Ta, W. Liu, D. Gao, G. Wang and X. Bao, *Adv. Mater.*, **32**, 1906193 (2020).
57. O. Kwon, K. Kim, S. Joo, H. Y. Jeong, J. Shin, J. W. Han, S. Sengodan and G. Kim, *J. Mater. Chem. A*, **6**, 15947 (2018).
58. J. Ko, H. Kwon, H. Kang, B.-K. Kim and J. W. Han, *Phys. Chem. Chem. Phys.*, **17**, 3123 (2015).
59. K. Kim, S. Baek, J. J. Kim and J. W. Han, *Appl. Surf. Sci.*, **510**, 145349 (2020).
60. S. Joo, O. Kwon, K. Kim, S. Kim, H. Kim, J. Shin, H. Y. Jeong, S. Sengodan, J. W. Han and G. Kim, *Nat. Commun.*, **10**, 697 (2019).
61. H. Han, J. Park, S. Y. Nam, K. J. Kim, G. M. Choi, S. S. P. Parkin, H. M. Jang and J. T. S. Irvine, *Nat. Commun.*, **10**, 1471 (2019).
62. H. Lv, L. Lin, X. Zhang, D. Gao, Y. Song, Y. Zhou, Q. Liu, G. Wang and X. Bao, *J. Mater. Chem. A*, **7**, 11967 (2019).
63. Y.-R. Jo, B. Koo, M.-J. Seo, J. K. Kim, S. Lee, K. Kim, J. W. Han, W. Jung and B.-J. Kim, *J. Am. Chem. Soc.*, **141**, 6690 (2019).
64. T.-S. Oh, E. K. Rahani, D. Neagu, J. T. S. Irvine, V. B. Shenoy, R. J. Gorte and J. M. Vohs, *J. Phys. Chem. Lett.*, **6**, 5106 (2015).
65. D. Ess, L. Gagliardi and S. Hammes-Schiffer, *Chem. Rev.*, **119**, 6507 (2019).

Jeong Woo Han is currently an Associate Professor of Chemical Engineering at Pohang University of Science and Technology (POSTECH), South Korea. He also holds an Editor position of *Molecular Catalysis* published by Elsevier since 2017. Before joining POSTECH in 2018, he was an Assistant/Associate Professor at the University of Seoul, South Korea. He obtained his PhD at Georgia Institute of Technology in 2010 under the guidance from Prof. David S. Sholl, who is now School Chair of Chemical and Biomolecular Engineering at Georgia Tech, focusing on computational catalysis and surface chemistry. From 2010 to 2012, he was also a postdoctoral associate at MIT who worked for Prof. Bilge Yildiz in Nuclear/Materials Science and Engineering. His current research area is computational modeling of catalysis and energy materials such as automotive catalysis, fuel cell electrodes, liquid organic hydrogen carrier, and single atom catalysis, and so on. He has published more than 110 SCI(E) papers. Since 2020, he has been elected as a member of Young Korean Academy of Science and Technology.